Electrostatic Actuation and Electromechanical Switching Behavior of One-Dimensional Nanostructures

Arunkumar Subramanian,*,†,‡ Andreas R. Alt,§ Lixin Dong,†,∥ Bradley E. Kratochvil,† Colombo R. Bolognesi,§ and Bradley J. Nelson*,†

†Institute of Robotics and Intelligent Systems, ETH Zurich, 8092 Zurich, Switzerland, ‡Center for Integrated Nanotechnologies, Sandia National Laboratories, Albuquerque, New Mexico 87185, §Laboratory for Electromagnetic Fields and Microwave Electronics (IfH), THz Electronics Group, ETH Zurich, 8092 Zurich, Switzerland, and ∥Electrical and Computer Engineering, Michigan State University, East Lansing, Michigan 48824

ABSTRACT We report on the electromechanical actuation and switching performance of nanoconstructs involving doubly clamped, individual multiwalled carbon nanotubes. Batch-fabricated, three-state switches with low ON-state voltages (6.7 V average) are demonstrated. A nanoassembly architecture that permits individual probing of one device at a time without crosstalk from other nanotubes, which are originally assembled in parallel, is presented. Experimental investigations into device performance metrics such as hysteresis, repeatability and failure modes are presented. Furthermore, current-driven shell etching is demonstrated as a tool to tune the nanomechanical clamping configuration, stiffness, and actuation voltage of fabricated devices. Computational models, which take into account the nonlinearities induced by stress-stiffening of 1-D nanowires at large deformations, are presented. Apart from providing accurate estimates of device performance, these models provide new insights into the extension of stable travel range in electrostatically actuated nanowire-based constructs as compared to their microscale counterparts.

KEYWORDS: carbon nanotubes · nanoelectromechanical systems · electrostatic actuation · pull-in GAP · shell engineering

Low-dimensional, finite-molecular structures, both in 1- and 2-D,[1,2] possess a number of important attributes such as low-mass, high surface area, atomic-scale geometric tolerances, and chemical purity. Processes for synthesizing these nanoscale building blocks from a number of material systems such as carbon,[1,2] semiconductors,[3] metal oxides[4] and III−V compounds[5] have been developed over the past decade. These nanoconstructs are expected to enable advances in diverse technological domains such as mechanics, electronics, photonics, energy transport/storage/conversion, manipulation, and sensing.

Carbon nanotubes (CNTs)[1] are 1-dimensional, cylindrical elements that have been demonstrated to possess unique elastostatic deformation mechanics. As nanomechanical elements, these condensed tubules of carbon outperform other materials in 1-D due to the exceptionally strong C−C covalent bonds between sp^2 hybridized atoms within these structures. This includes robust strain relaxation capabilities, nonlinear force-deflection curves, high stiffness and strength, and extremely high natural frequencies due to their low mass.[6,7] Sensors responding to diverse stimuli such as pressure, force, and mass,[8,9] resonators,[10] nanoradios,[11] nanomotors,[12] electromechanical switches, and nanorelays[13−20] are a few examples of devices that have exploited the favorable nanomechanical properties of CNTs. Furthermore, the high frequency (GHz regime) operation of nanomechanical switches has been investigated[18,20] demonstrating their potential for logic elements, memories, pulse generators, and current/voltage amplifiers.

This paper presents an electrostatically actuated, three-state nanoswitch based on a doubly clamped, individual multiwalled carbon nanotube (MWNT). In addition to switching performance, we also provide insight into the fundamental electrostatic actuation regime of one-dimensional nanostructures through the experimental and theoretical investigation of these constructs. While switches based on nanowires have been reported in refs 13−20, the research contributions of this effort span the following: (1) batch-fabricated devices with a three-state device architecture that exhibits low-voltage (consequently, low-power) operation, (2) demonstration of shell engineering as a tool to tune the nanomechanical clamping configuration, stiffness and actuation voltage in MWNT-based electrostatic actuators/switches, (3) detailed analysis of device operation

*Address correspondence to: asubram@sandia.gov, bnelson@ethz.ch.

Received for review April 30, 2009 and accepted September 2, 2009.

Published online September 9, 2009. 10.1021/nn900436x CCC: $40.75

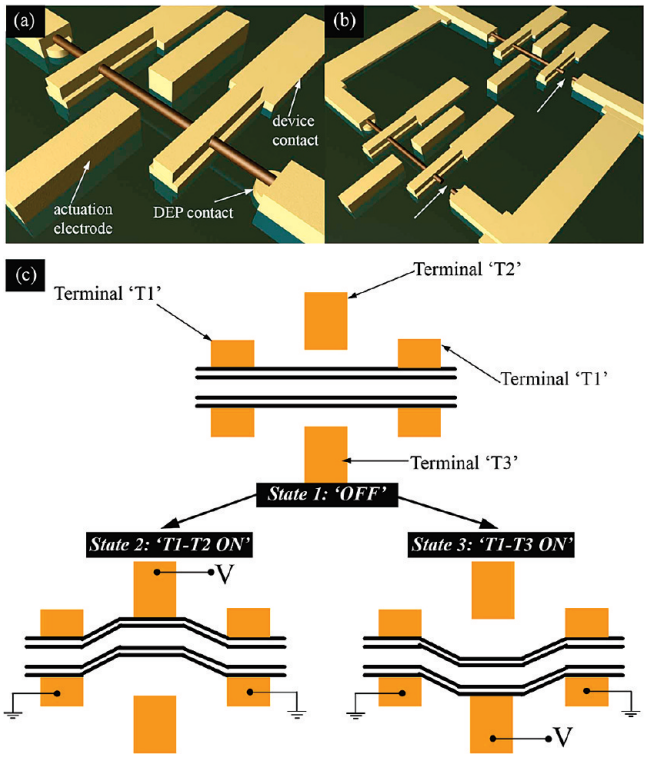

Figure 1. Three-state NEMS switch. (a) Device schematic with the actuation electrodes, DEP biasing, and device contacts labeled. (b) One of two techniques employed to probe individual devices within an array without intereference from the remaining NTs. Two devices in the array with the interconnection *via* DEP contacts are shown here. The white arrows point to breaks in the nanotubes engineered by driving currents in order to isolate devices from each other. (c) Three states of the device. The "OFF" state in the absence of external bias is shown on top. The "T1−T2 ON" state when a voltage is applied to terminal T2 is shown in bottom left. The bottom-right image illustrates the "T1−T3 ON" state when a bias is applied to terminal T3.

(including a parametric analysis) and prediction of extended travel range before the onset of "pull-in" within the performance regimes of nanowire-based electrostatic actuators/switches, (4) analysis of device failure modes, and (5) nanoassembled architectures that permit individual probing of one NT device at a time without crosstalk from other tubes originally assembled in parallel.

RESULTS AND DISCUSSION

The structure of this three-state, electrostatically actuated NEMS switch is shown in Figure 1a. The nanoconstruct consists of a MWNT that bridges four metallic contacts after DEP assembly. The nanotube remains flat and fully suspended in air in each of the three regions between metallic contacts. The two distal contacts, referred to as "DEP contacts", are employed to generate force fields during NT assembly and are shared by all NTs in a fabricated array of devices. The two inner contacts are used to bias the nanotube during device operation. Each pair of these device contacts is connected locally to only one NT within the array and is not directly wired to the remaining NTs (see Figure 1a). Each of these contacts has two layers of metallic pads (made of Cr/Au) between which the nanotube is sandwiched to ensure good electrical contact. In addition, two metallic electrodes are defined in proximity to the NT (within a distance of 10−30 nm) and are located on either side of the tube at its midlength. These two actuation (or gate) electrodes induce electrostatic forces on the suspended NT. The fabrication process employed to build these devices can be found in the methods section.

During device operation (shown in Figure 1c), the two biasing contacts are held at a common, ground potential and form the first terminal, T1, of the NEMS switch. The gate electrodes form the remaining two terminals (T2 and T3) of the switch. In the as-fabricated "off-state", the nanotube is not in physical contact with actuation electrodes, and the electrical circuit between terminals T1−T2 and T1−T3 remain open. When a potential is applied to one of the actuation electrodes, the resulting attractive electrostatic force deforms the nanotube. While the nanotube deformation increases with applied voltage, there exists a certain threshold bias beyond which the electrostatic force is far higher than the restoring elastostatic force. Beyond this characteristic threshold, called the "pull-in" voltage, the nanotube−electrode gap is closed and the switch is turned "ON" (Figure 1c). Thus, the circuit between terminals T1−T2 and T1−T3 can be turned ON by applying the pull-in voltage at the respective actuation electrodes. When a potential is applied to both the actuation electrodes simultaneously, the nanotube experiences competing electrostatic forces from both sides and the switch remains turned "OFF". An electromechanical switch has previously been reported[19] with electrode geometry similar to ours in all respects, except for the fact that we have four NT contacts as opposed to two (rationale for this key difference is explained later). Another difference with our report relates to the actuation mechanism. Reference 19 employs electrostatic repulsion forces to control the device state and requires three control signals. On the other hand, the actuation mechanism presented in this effort is simpler (requires only two control signals as against three) and achieves switching using electrostatic attraction forces without any trade-offs in terms of performance metrics. The lower actuation voltages in ref 19 (3−4 V as opposed to the 6.7 V average reported here) is a result of device scaling (NTs are twice as long as ours), and is not caused by any actuation or device architecture efficiencies.

Because all NTs in an array are connected in parallel through DEP contacts, it is essential to isolate devices from each other and enable individual device characterization without cross-talk. This is achieved using one of two techniques: (1) by holding the two device contacts at a common potential (This common potential is one of two potentials applied to electrostatically actuate the device. This insures that there is no current flow

through the remaining NTs in the fabricated array (by electrically shorting their contacts)); or (2) by etching all shells in one (or both) of the NT segments near the DEP contacts. This is accomplished by a single-step breakdown of all NT shells using Joule heating induced by a high current pulse and has previously been demonstrated to create bidirectional bearings.[21] Figure 1b schematically illustrates two devices in an array that are decoupled in this manner. The second option is useful in cases where we wish to drive currents and thin the NT (using current driven shell engineering as reported in refs 21−24) between device contacts in order to tune its mechanical stiffness and clamping configuration prior to actuation/switching.

SEM images of the array design and fabricated structures can be seen in Figure 2a−e. Figure 2f shows the NT of panel b after Joule heating has broken the tube near the right device contact and decoupled it from the rest of the NTs in the array. This image was taken after a number of switching tests. Changes in the NT−metal contact interface at terminals T2 and T3 due to switching are evident in this image.

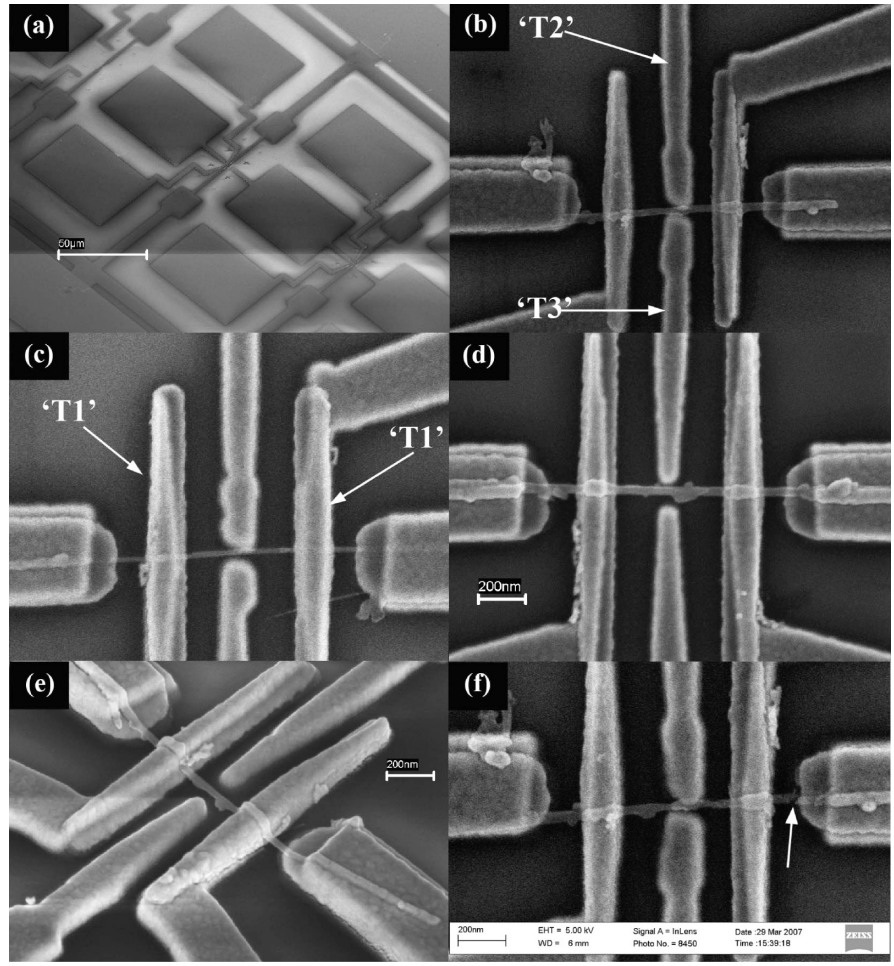

Figure 2. Three-state NEMS switches. (a) Device array design. (b−d) Top-view of a few devices. The labeling of terminals T2 and T3 is shown in panel b. Panel c illustrates the labeling of terminal T1, which represents the two device contacts held at an identical potential. Also, the asymmetry in NT-electrode gap at terminals T2 and T3 is evident from these images. (e) SEM image of a fabricated device taken at a stage tilt of 40°. (f) SEM image of device in panel b after the NT is decoupled from the array using electric breakdown near a DEP biasing contact (break indicated with an arrow). Note: This image was taken after a few switching cycles and changes in NT/electrode interface (due to switching) are evident.

In the constructed devices, the active length of suspended MWNTs is 425 nm (measured between device contacts), while the outer diameter ranges between 8 and 20 nm. The NT−electrode separation is designed to be 30 nm for each of the two actuation electrodes situated on either side of the NT. However, the actual gaps are not equal on both sides and tend to be smaller than the design value on at least one side. This is due to two factors: (1) lithography bias caused by overexposure in the central device region which has a high pixel-density; this results in a reduction of the NT-electrode gap on both sides; and (2) ~10 nm alignment inaccuracy between the first and second metallic layers defined by EBL; this results in nonequal device gaps at terminals T2 and T3 (terminal labeling can be found in Figure 2b,c and is consistent with the definition in Figure 1c). The exact value of this initial NT−electrode separation is difficult to determine within the limits of SEM imaging due to increased electron scattering at the NT and actuation electrode side-walls. This is further accentuated by the inclination of electrode side-walls and the extremely small gaps, which have not been encountered in previous reports. We would like to emphasize that the small gaps achieved in this effort have been instrumental in low voltage device operation (within 5 V or CMOS-level in 10 out of 29 devices). For instance, in MWNT devices reported in refs 13−15, the gaps varied between 80 and 900 nm resulting in switching voltages of 10−30 V.

There is apparent overlap between the NT and actuation electrode in some SEM images showing the top-view of devices. Though the possibility of metallic traces on NT edges near the actuation electrodes cannot be ruled out (due to the wet chemistry within extremely small gaps in the lift-off process), the NTs were not welded to the actuation electrode during fabrication. In every measured device, this existence of separation has been confirmed using $I-V$ plots where the device turned ON only after the application of a voltage in the 2−15 V range. This apparent overlap in the top-view can be attributed to two factors: (1) the sloped profile

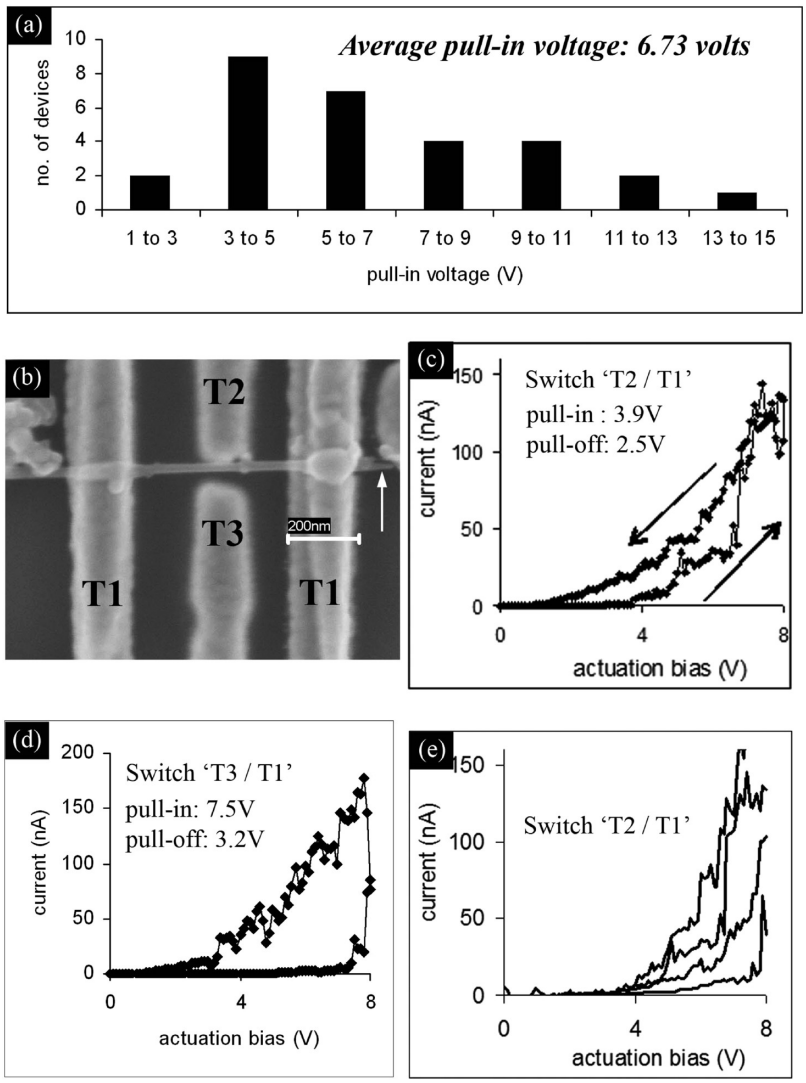

Figure 3. Device characterization. (a) Distribution of the measured ON state voltage for 29 switches. (b) SEM image of a device with terminal labeling shown. The arrow points to a current induced break in the NT to decouple it from the array. (c) I−V characteristics of the switch between terminals "T1−T2". The plot indicates electromechanical hysteresis inherent in these devices. The arrows point to the increasing and decreasing voltage parts of the curve. (d) I−V characteristics of the switch between terminals T3−T1. (e) Device operation over four cycles shown to demonstrate the repeatability in device behavior. It is evident that while the pull-in voltage remains within a small range, the tunnelling currents in the ON state lie within a factor of 3.

of the electrode side-walls (a cross-sectional schematic in inset of Supporting Information, Figure S1a highlights this aspect), and (2) increased electron scattering at NT and electrode side-walls during SEM imaging. Apart from the electrical measurements showing an open circuit until threshold bias for electromechanical switching, further evidence in support of this argument can be found in Supporting Information, Figure S1.

Switching characteristics were investigated for 24 devices. The electrical measurements were performed within a vacuum chamber. In five of these devices, three-terminal operation could be established. In the remaining 19 devices, only one of the two switching circuits could be measured owing to the following factors. In some cases, the device failed after several switching cycles due to a breakdown of the NT or the actuation electrode. In other devices, either the NT was welded to one of the electrodes after switching due to long device ON times, or the assembly of multiple nanotubes at a single device location prevented the definition of one of the two actuation electrodes (further information on device failure modes can be found in Supporting Figure S2). Thus, a total of 29 switches (two each in the five devices that exhibited 3-state operation, and one each in the remaining 19 devices) were characterized. The distribution of voltages required to switch these devices to the ON state is summarized in Figure 3a. From this plot, it can be seen that the average pull-in voltage was 6.73 V and, in 10 of 29 devices, the threshold bias was lower than 5 V.

An SEM image of a device that exhibited three-terminal operation is shown in Figure 3b and the performance characteristics of this device are shown in Figure 3(c−e). The biasing approach involved increasing the voltage from 0 to V_{max} in 100 mV increments during the first half of the cycle and, then, decreasing the voltage back to 0 in the second half. This biasing method provides useful insight into the electromechanical hysteresis that is introduced by van der Waals forces. The $I-V$ plot during the switching transition between terminals T2 and T1 is shown in panel c. From this curve, it is evident that pull-in occurs at 3.9 V while the pull-off event occurs at 2.5 V. This is due to van der Waals interactions, between the NT and electrode after pull-in, that oppose the elastostatic restoring force during the pull-off transition. In addition, the nonlinear characteristic of these $I-V$ plots is a signature of a tunneling interface at the NT-electrode contact and is similar to behavior observed in previous reports.[13−15] The $I-V$ plots measured during the switching transition between terminals T3 and T1 can be seen in Figure 3d. The pull-in voltage for this terminal was found to be higher at 7.5 V. This is to be expected due to larger NT-electrode separation at this terminal as compared to terminal T2. The robustness of the devices was further investigated by repeated switching, and the results from these measurements are shown for four cycles (for switching induced by terminal T2) in Figure 3e. It can be observed from this plot that the turn-on bias remains repeatable. However, the currents after pull-in vary within a factor of 3. This indicates changes at the NT−electrode interface during successive cycles due to high power dissipation at the contacts. This argument is confirmed by the

images shown before and after switching for the NT in panels b and f of Figure 1. The possibility of local removal of a few shells at the interface leading to this behavior can also not be ruled out.

One important aspect in the measurements discussed above is the small (80 μs) time steps between 100 mV increments during the biasing cycle. This results in the NT remaining in the ON state for time scales of the order of a few milli-seconds. If the ON times are longer (on the order of 0.2−1 s), the high device contact resistance causes the gold to locally melt and the metal grain boundaries reflow at the NT−electrode interface resulting in increased contact area and reduced resistance. A direct consequence of this is that the NT−electrode van der Waals interactions are significantly higher, and result in the NT remaining welded to the gold surface even after the excitation bias is removed. Further information on this and other device failure modes is provided in Supporting Information, Figure S2.

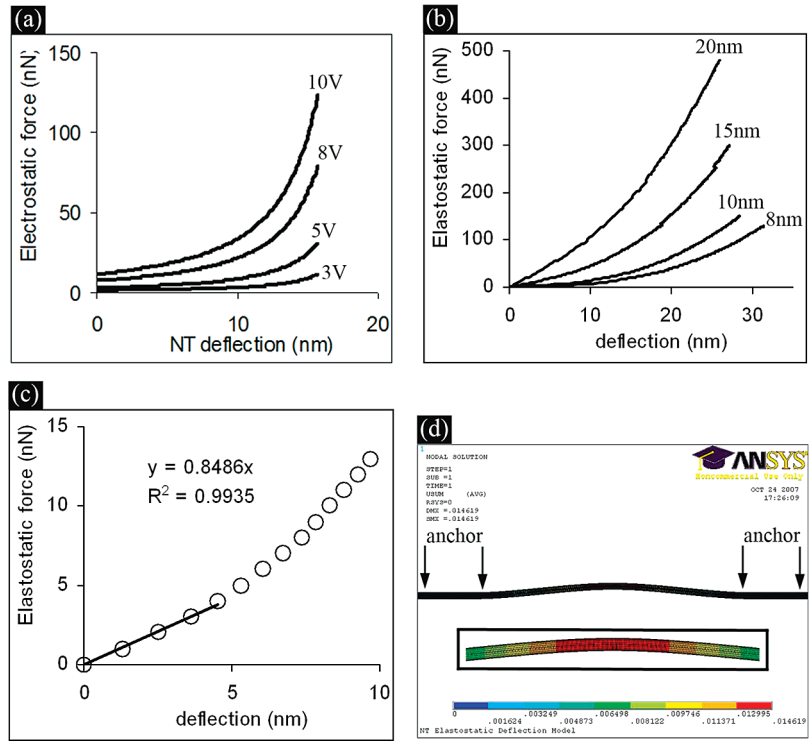

Figure 4. (a) Plots of electrostatic actuation forces as a function of MWNT deflection at 3, 5, 8, and 10 V. The initial device separation is assumed to be 20 nm and these plots are shown until a NT deflection of 16 nm. (b) Elastostatic force *vs* deflection plots of nanotubes with four different diameters computed using a finite-element model built in ANSYS. The number of shells in each of these tubes was assumed to be 10. The labels shown along the curves indicate the NT outer diameter. (c) A closer view of the plot in panel a for a 10 nm diameter tube in the low deformation regime. The circles denote the simulation values, and a linear fit for deformations below 5 nm is also shown (the legend indicates the line equation and its fit to the plot). (d) ANSYS contour plot showing the deformation profile along the length of a 10 nm diameter nanotube for an applied force of 30 nN. A closer view of this plot in the nanotube midlength region is shown within inset.

When a voltage is applied at one of the actuation electrodes while holding the biasing contacts at ground potential, three types of forces are exerted on the nanotube: (1) electrostatic attraction force due to the opposite polarity charges induced in the NT and the electrode, (2) elastostatic restoring force caused by nanotube deformation, and (3) van der Waals attraction forces between the actuation electrode and the nanotube. The device state at an applied voltage as well as its performance metrics are determined by the ability to modulate and control these forces using suitable design parameters. Analytical and finite-element models were used to estimate these forces within the electrostatic actuation regimes of fabricated switches. In the first part of this discussion, a MWNT (10 nm outer diameter) that is fabricated with an initial overlap and separation distances of 100 and 20 nm, respectively, with respect to the actuation electrode is employed as a case study to illustrate the method employed for computing individual force components. In the next part related to device operation point and pull-in dynamics, this discussion is extended to demonstrate the influence of parameters such as NT diameter and initial separation.

The electrostatic force exerted on the nanotube can be derived from an analytical capacitance model.[25] In the device geometry under consideration, a cylindrical conductor (MWNT), of length l_{NT} and outer radius R, is spatially separated from an actuation electrode (gold) of length l_{act} by an initial design gap of g_0. As the nanotube deflects, its separation from the electrode is reduced and this separation is denoted by the variable g. For an applied external voltage V, the electrostatic force acting on the nanotube at a gap g can be computed[26] as

$$F_{elec}(g) = \frac{dE_{elec}}{dg} = \frac{-\pi\varepsilon_0 V^2 l_{act}}{RA\log^2\left(1 + \frac{g}{R} + A\right)} \qquad (1)$$

where

$$A = \sqrt{\frac{g(g + 2R)}{R^2}}$$

In the above expression, ε_0 represents the permittivity of free space (8.85×10^{-12} F/m) and E_{elec} represents the electrostatic energy stored in the system. The negative sign indicates that the electrostatic force is attractive. By substituting $g = g_0 - d$, the electrostatic force can be expressed as a function of NT deflection d using the following relation:

$$F_{elec}(d) = \frac{-\pi\varepsilon_0 V^2 l_{act}}{RB\log^2\left(1 + \frac{g_0 - d}{R} + B\right)} \qquad (2)$$

where

$$B = \sqrt{\frac{(g_0 - d)(g_0 - d + 2R)}{R^2}}$$

For the devices employed in this effort, $I_{act} = 100$ nm and the initial separation g_0 is between 10 and 30 nm. The outer radii R of the NTs (arc-produced and obtained from MER Corp.) are in the 4−10 nm range. The typical profile of the electrostatic force as a function of NT deflection is shown in Figure 4a for a range of external biases applied at the actuation electrode. These curves were computed for an NT with an outer diameter of 10 nm. The initial separation was assumed to be 20 nm.

One important assumption in this model is that the NT−electrode gap remains uniform over the length of the nanotube that experiences actuation forces. As will be evident from the elastostatic models in the following subsection, this would overestimate the electrostatic forces in the large deformation regime that occurs when the nanotube is in proximity to the electrode (within a few nm). However, this assumption is valid for estimating pull-in voltages and gaps, where the nanotube−electrode separation is larger than the NT deformation in the region where electrostatic forces are exerted.

Previous reports indicate that the mechanics of nanotubes exhibit continuum behavior when tube lengths are on the order of hundreds of nm. Some of these efforts have employed continuum beam theory which assumes that all the strain energy in a deformed nanotube is stored in the bending mode.[7,13,26] This simple linear model represents a reasonable assumption for thick MWNTs (with a diameter of 20 nm or more) undergoing deformations smaller than their radius. However, when the nanotube diameter is small, resulting in ultralarge aspect ratios, or when the deformations are large, the force−deflection behavior is highly nonlinear. This is due to the nanotube behaving like a rope or a string, where the strain energy is stored in both the tension and bending modes, and has been experimentally observed in ref 8. Thus, more sophisticated models are required to predict the large-deformation mechanics that is encountered within our device actuation regime. Numerical models that account for nonlinear mechanics in SWNT resonators have been reported previously.[27,28] Also, the impact of nonlinear mechanics on the elastostatic and electromechanical behavior of MWNTs has been investigated using molecular dynamics and continuum methods.[29,30]

In this effort, a finite-element model built in ANSYS is used to estimate the elastostatic deformation of NTs. The "BEAM188" element, which supports large deformation analysis in high aspect ratio beams is used to mesh the NT geometry. The model takes into account the tension component induced at large deformations and the resulting stress-stiffening effects, which are common in structures such as cables and membranes. The typical force−deflection plots estimated by this model are shown in Figure 4b. This computation involved 10-shell MWNTs with outer radii ranging between 4 and 10 nm and a suspended length (between device contacts) of 425 nm. In addition, the average value of Young's modulus of nanotubes within our sample is assumed to be 0.6 TPa. Apart from being within the range of measurements previously reported,[6,7,31,32] this assumption has also been validated with experimental observations from NTs tested in this effort (as discussed later).

The deflection profile along the length of this doubly clamped structure is shown in Figure 4d for a load of 30 nN applied on a 10 nm diameter tube. In this model, the load is applied uniformly over a 100 nm region located at NT midlengths. This region coincides with the location of electrostatic forces in device designs. An interesting aspect that emerges from these models is the linearity of the force−deflection behavior in the small deformation regime. The extent of this linear regime is strongly dependent on the NT diameter. For instance, the behavior of a NT with 10 nm outer diameter is linear until a deformation of 5 nm (shown in Figure 4c), while it extends up to a deformation of 9 nm in the case of a NT with an outer diameter of 20 nm. Thus, the linear regime extends up to deformations of the order of NT radius.

The NT−electrode van der Waals forces can be estimated using the Lennard-Jones model.[33] The Lennard-Jones potential between two atoms separated by a distance r is given by

$$\phi = 4\varepsilon\left[\frac{\sigma^{12}}{r^{12}} - \frac{\sigma^{6}}{r^{6}}\right] \quad (3)$$

where ε represents the well depth and σ is a geometric parameter that is related to the equilibrium distance x_0 (by the relation $x_0 = 2^{1/6}\sigma$). When the gap between gold and carbon atoms is higher than 0.5 nm, as is the case with the 10−30 nm initial separation employed in devices, the repulsive component of the Lennard-Jones potential in eq 3 can be ignored. Thus, the total NT−electrode van der Waals force can be computed by the pairwise summation of attractive forces for each atom. An alternative approach would involve a continuum model that computes the double-volume (or surface) integral of the Lennard-Jones potential. As reported in ref 26, the van der Waals force per unit length can then be obtained from the derivative of the energy, and can be written as

$$\frac{F_{vdw}}{L} = -\frac{CD}{F} \quad (4)$$

where

$$D = 8g^4 + 32g^3R + 72g^2R^2 + 80gR^3 + 35R^4$$

$$C = 4\varepsilon_{eff}\sigma_{eff}^{6}\lambda^2\pi^2R\sqrt{g(g + 2R)}$$

$$F = 2g^5(g + 2R)^5$$

and where λ is a parameter that is dependent on the surface density of atoms. Since the device under consideration represents a two-component system where the van der Waals interactions occur between gold and carbon atoms, the values of geometric parameter and well depth in eq 3 are replaced by the effective values, σ_{eff} and ε_{eff}, respectively, in eq 4. These parameters can be calculated using techniques outlined in refs 34 and 35 for two-component interactions. From computations using eq 4, we find that these van der Waals interactions are only dominant over a very short-range. For instance, the van der Waals force is about 4 orders of magnitude higher at a separation of 0.5 nm as compared to that at a separation of 20 nm (7.9 μN/μm *vs* 0.5 nN/μm). Assuming an interaction length of 100 nm at large gaps (which is the electrode dimension used in devices), the NT-electrode van der Waals force at a 20 nm gap can be computed as 54.27 pN. This is 3 orders of magnitude lower than the electrostatic and elastostatic forces (which were shown previously in Figure 4). Thus, the van der Waals forces can be neglected during device operation at gaps larger than 0.5 nm, as is the case with the OFF-to-ON transition and pull-in regimes.

From the previous discussion, it is clear that van der Waals forces can be neglected in estimating the device behavior before the onset of pull-in. Thus, for a given voltage, the nanotube deflection and device operating point is determined by the region where the electrostatic and elastostatic curves meet. Since there is no closed form solution to this problem, a MATLAB code was developed to determine the device operating point. The nonlinear force-deflection profile of the NT (computed using ANSYS) and the electrostatic force model given in eq 2 serve as input to this code. The metrics calculated include device operating point (NT deflection) at a given voltage, and for a given device geometry, voltage required for pull-in and the NT deflection at this point. The performance metrics computed are for a 10 nm outer diameter MWNT with a 20 nm initial separation from the actuation electrode. Figure 5a shows the force curves as a function of deflection when the applied voltage is 5 V. From this figure, it is evident that the electrostatic and elastostatic curves meet at two points. However, the lower deflection solution represents the physical behavior since the higher deflection operating point requires a transition through energetically unfavorable intermediate positions (where the restoring force is higher than the actuation force). Thus, the nanotube is deflected by 6.03 nm when a bias of 5 V is applied to the actuation electrode. When the external bias is increased, a value exists at which the two force curves are asymptotic. At voltages beyond this, the electrostatic force is higher than the elastostatic force for all nanotube positions. This voltage is referred to as the pull-in or ON voltage of the device. At a higher bias, the NT always remains in contact with the electrode. The force curves at a pull-in voltage of 6.5 V for the device under consideration are shown in Figure 5b.

Figure 5c shows the variation of switching bias as a function of the initial gap between the NT and electrode. These plots are shown for NTs with three different diameters (8, 15, and 20) that cover the range of NT sizes found in the sample used in this effort. For each of these NT diameters, the number of shells is assumed to be 10. In the absence of direct data on the number of shells within each individual tube (due to the incompatibility of our devices for TEM imaging), this value in our models has been assumed to represent an average number that lies within the manufacturer's (MER Corp.) specification of 6−20 shells. The experimentally observed voltage spectrum for device switching varied between 2 and 15 V and is indicated by a shaded gray region in Figure 5c. It is evident from this figure that the

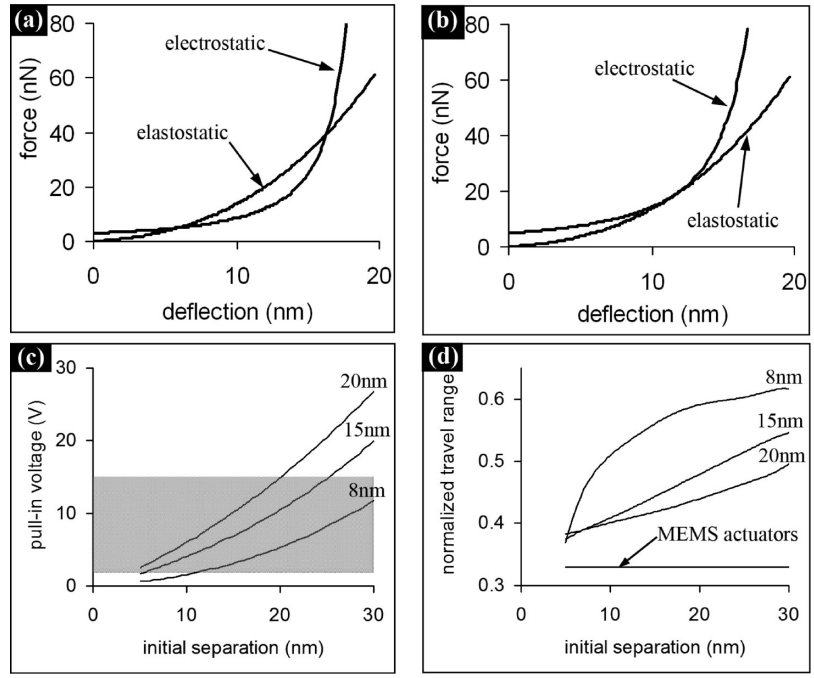

Figure 5. (a,b) Switch operation and pull-in analysis for a 10 nm outer diameter MWNT with an initial separation of 20 nm from the actuation electrode. Panel a shows typical force curves before onset of pull-in, and panel b shows force curves at the pull-in point. It can be seen that the electrostatic and elastostatic curves are asymptotic at pull-in. (c,d) Pull-in voltage and travel range computation. Panel c shows the variation of pull-in voltage as a function of the initial NT-electrode separation for NTs with 8, 15, and 20 nm outer diameter. The shaded region indicates the range of voltages measured in 29 devices. Panel d shows the variation of normalized travel range before onset of pull-in as a function of initial NT-electrode separation for NTs with 8, 15, and 20 nm diameter.

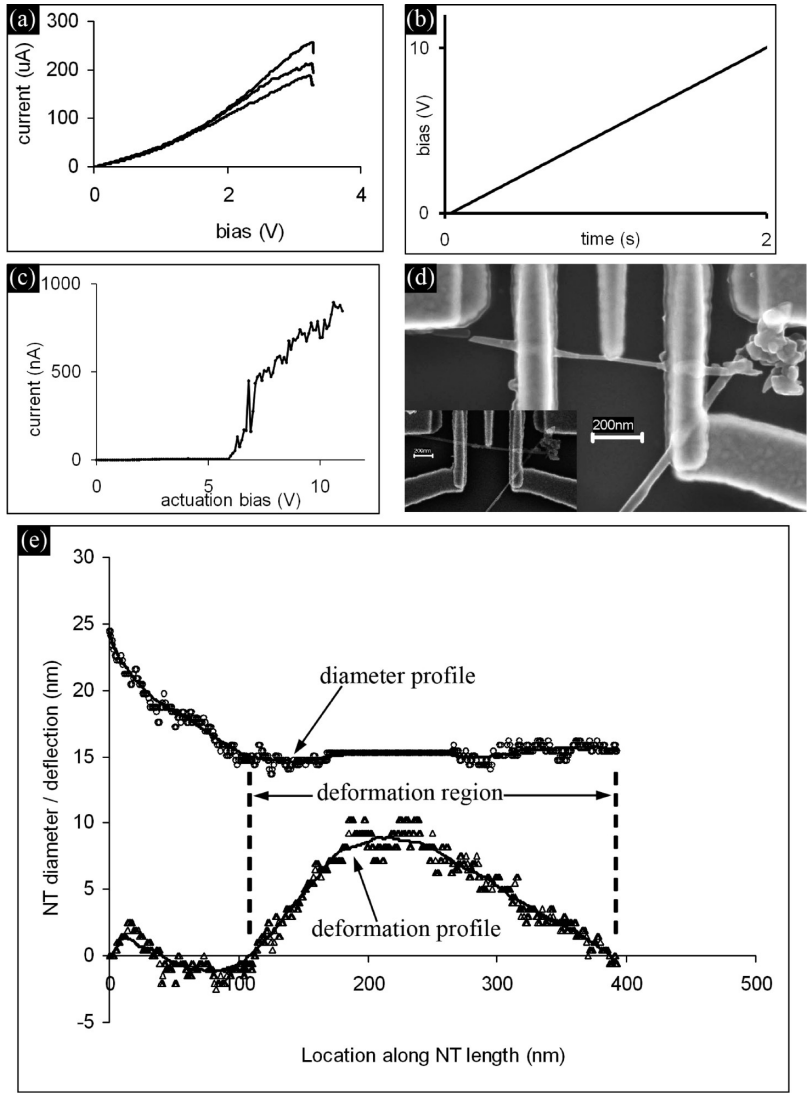

Figure 6. (a) *I*−*V* measurements during shell thinning experiments. (b) The actuation voltage *vs* time plot which shows that the voltage is increased slowly. In this case, the NT remains ON for ~0.8 s. (c) *I*−*V* plot showing the switching characteristic of the device. It can be seen that while pull-in occurs at 5.9 V, there is a step-like increase in current at 7.1 V. Also, the *I*−*V* characteristic is linear beyond 7.1 V due to the NT being welded onto the electrode. (d) Top-view of the device in which the NT is welded to the electrode after a switching event. An image of the device prior to shell engineering and actuation is shown in inset. (e) Diameter and deformation profile extracted along the length of the NT using an image processing code developed in MATLAB. The plots show both the raw data as well as a curve fit based on moving average approximation to filter the noise. From this panel, it is evident that the elastostatic strain is absorbed entirely in the thinned NT segment and the tube effectively behaves as a 15 nm diameter element with a 278 nm suspended length.

values predicted by the models lie within the experimentally observed voltage spectrum. This also indicates that the value of 0.6 TPa, which is used as the average NT Young's modulus in these computations, represents a reasonable assumption.

Another significant attribute of electromechanical actuation using 1-D nanoscale elements that emerges from these models is the extended travel range before onset of pull-in. In the case of MEMS devices, the parallel plate capacitance behavior and the constant stiffness characteristic of micromechanical springs result in the initiation of pull-in at $2g_0/3$ (g_0 represents the initial separation). This implies that if micromachined elements are used as springs in electrostatic actuators, the stable travel range that could be realized is one-third of the initial gap. This is an important metric that must be optimized for a number of transduction applications such as microfluidic elements and Fabry−Perot filters among others.

In the case of MWNTs, we find that this travel range is significantly extended before the onset of pull-in. This is attributed to the nonlinear force-deflection relationship which increases the elastostatic forces at large deformations. As a result, larger voltages and deflections are required before pull-in occurs in MWNT-based electrostatic actuators. This characteristic can be clearly seen in the plots shown in Figure 5d where the normalized travel range (defined as the ratio between the deflection before pull-in and the initial NT-electrode separation) is plotted as a function of initial gaps. The normalized travel range increases with decreasing diameter and increasing initial separation. This is to be expected since nonlinear deformation effects occur only in high-aspect ratio or large deformation regimes. Thus, the use of 1-D nanostructures as strain-absorbing mechanical elements in electrostatic actuators can lead to an extended travel range. This extension of travel range is expected to occur for all 1-D nanowires (and not just MWNTs), irrespective of the nanomaterial. The simulations presented here are the first predictions of this improved performance regime in NEMS actuators.

Previous reports (from our as well as other research groups) have demonstrated the possibility of etching a few MWNT shells,[21−24] starting from the outermost one and proceeding inward using Joule heating induced electric breakdown. By monitoring the NT current, this technique could be used to thin a nanotube and is possible only in MWNTs (among all known nanomaterials) due to their unique nested shell architecture. Using experimental and simulation results from a NT device, we demonstrate the utility of this technique to tune the MWNT diameter (thereby, its stiffness), mechanical clamping configuration at anchors, and power required for actuation/switching. The removal of one or a few outermost shells after device fabrication can also be used to clean up the NT from any impurities during the fabrication process. This results in the use of pristine in-

ner shells for switching experiments resulting in lower contact resistances.

The outer diameter of the NT under consideration is estimated to be 24 nm (extracted using an image processing code written in Matlab). Prior to shell removal, the NT did not exhibit any switching until an actuation voltage of 15 V (higher voltages were not further applied to avoid the possibility of breakdown of metallic electrodes). As a first step in this analysis, the NT was completely decoupled from the array (*via* a single-step electric breakdown of all shells near DEP contacts, as illustrated previously in Figures 2f and 3b). Next, some of the outer NT shells were etched in the region between the two device contacts by driving currents between them, and the *I*−*V* plots that were used to monitor this etching process are shown in Figure 6a. After this thinning step, the NT diameter is extracted from the image processing code to be 15 nm. It is important to note that breakdown of the NT in the region between device and DEP biasing contacts is essential to selectively thin the NT without influence from other NTs in the array. The floating electrode DEP technique that we have presented here is unique in that we assemble arrays of NTs where each tube bridges four spatially separated contacts and remains suspended in the interelectrode regions. This represents an important improvement over previous efforts which have demonstrated arrays of NTs where each tube bridges only one or two metallic contacts.[18,36−38]

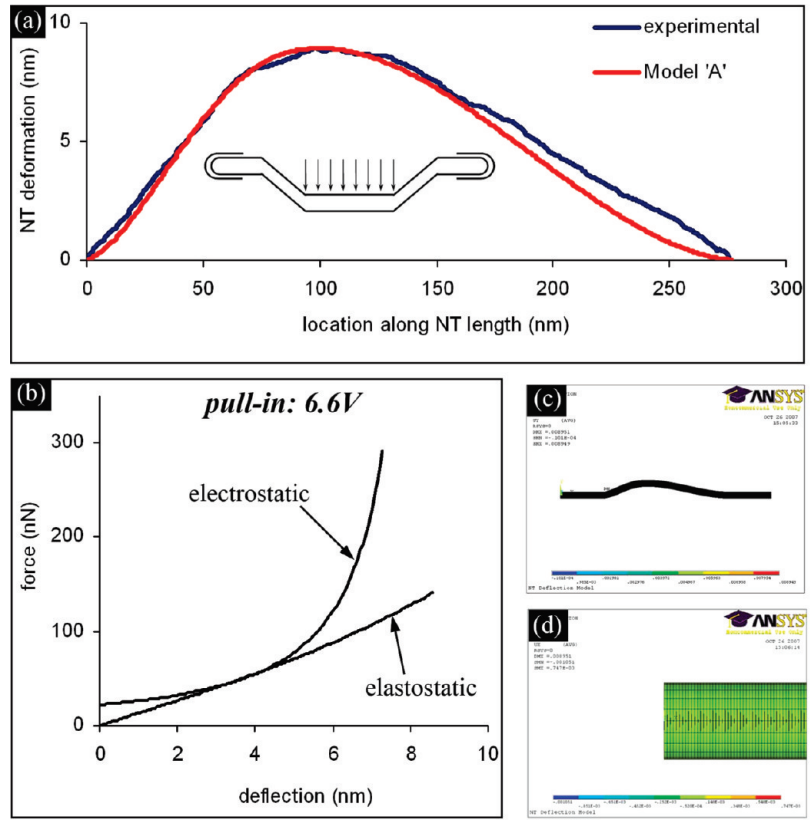

Figure 7. Results from modeling approach without shell sliding. (a) Comparison of the deformation profile obtained from this model against the experimental data. The inset highlights the boundary conditions assumed in this model. (b) Force curves at the pull-in voltage of 6.6 V predicted by this modeling approach. (c) Transverse deflection profile along NT length. (d) Plot showing the deformed surface and the undeformed edge at the left anchor point. It is hard to distinguish between the two since the two overlap completely confirming the fully fixed boundary condition assumed in this model.

After current driven shell etching, we investigated the nanomechanics of this modified structure by applying a long-duration bias to the actuation electrode, which causes the NT to remain welded to the electrode after switching (Figure 6b−d). The biasing approach employed involved increasing the voltage from 0 to 10 V over 2 s (unlike in the previous part of this report, this is a significantly longer biasing time). The applied actuation voltage as a function of time is shown in Figure 6b, while the *I*−*V* plots during the switching transition are shown in Figure 6c. As can be seen from these plots, the thinned device (with a NT diameter of 15 nm) switches to the ON state at 5.9 V. Thus, it is clear that thinning can be employed to realize low-power device operation. Another aspect of this biasing approach is that the device remains in the ON state for 0.8 s. This long ON state time causes the gold actuation electrode at the contact interface to melt, and the metal grain boundaries to reflow at the NT−electrode interface resulting in increased contact area and reduced resistance. A direct consequence of this is that the NT−electrode van der Waals interactions are significantly higher and result in the NT remaining welded to the gold surface even after the excitation bias is removed. From the *I*−*V* characteristic, it is evident that there is a steplike increase in current (measured to occur at about 235 milli-seconds after turning the device ON) accompanied with an ohmic-type behavior beyond this event, as would be expected due to the reduced contact resistance. The welded NT device after switching is shown in Figure 6d, while the device prior to shell thinning and actuation is shown in the inset. Though this represents a failure mode for nanoswitches, the deformed NT structure obtained using this experiment provides us with valuable information on the nanomechanics of shell engineered MWNTs.

The NT diameter and bending profile, shown in Figure 6e, were extracted from an SEM image using an image processing code developed in MATLAB. The diameter of the thinned NT portion is estimated to be 15 nm. One significant characteristic that emerges from this data is that the entire elastostatic strain energy is absorbed in the thinned, 15 nm diameter region. This can be seen from panel e, where the diameter and deformation profiles are shown in the top and bottom parts of the same plot. It can be seen that the nanotube deforms only in the 15 nm diameter segment (dotted lines are

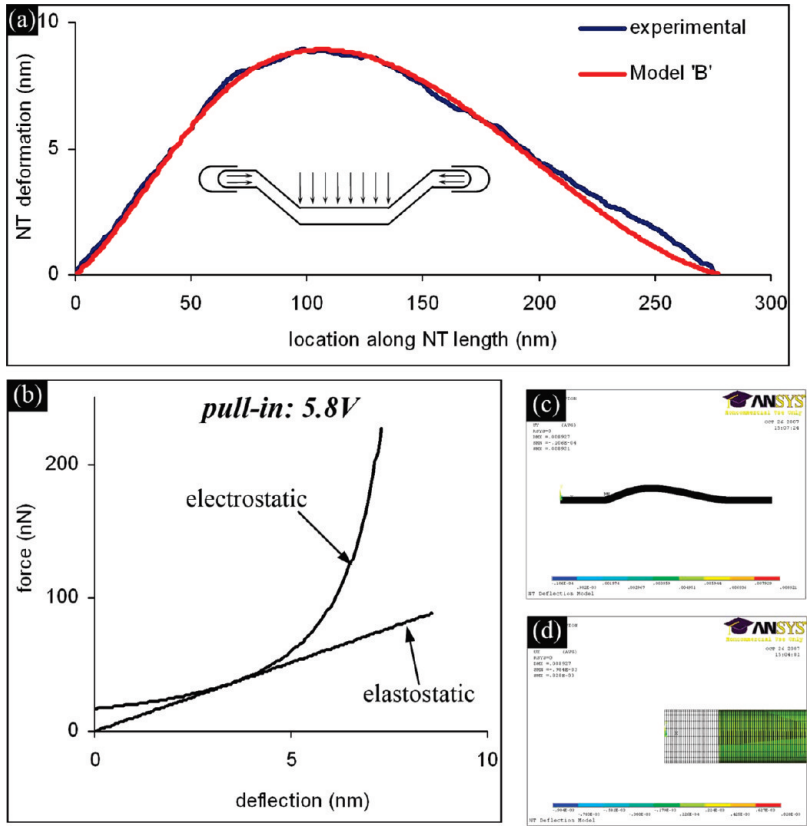

Figure 8. Results from modeling approach with shell sliding. (a) Comparison of the deformation profile obtained from this model against the experimental data. The inset highlights the boundary conditions assumed in this model where the core slides inside the outer housing. (b) Force curves at the pull-in voltage of 5.8 V predicted by this modeling approach. (c) Transverse deflection profile along NT length. (d) Plot showing the deformed surface (green) and the undeformed edge (grid lines in black) at the left anchor point. The model predicts a sliding distance of 0.2 nm in the axial direction.

drawn in this image to act as a pointer to the eye). Thus, the nanotube behaves effectively as a smaller diameter element with shorter active device length (computed to be 278 nm in this case).

Because of the possibility of intershell sliding at mechanical anchor points during deformation of this shell engineered structure, there are two possible boundary conditions depending on the extent to which shell sliding occurs. Both these possibilities have been investigated and the model estimates have been compared against the observed pull-in voltage/deformation profile. The results from these two modeling approaches are provided below.

Modeling results based on the fully fixed approximation (without shell sliding at anchors) at nanotube anchor points are presented first. In this approach, the nanotube is modeled as a 15 nm diameter, doubly clamped beam with a suspended length of 278 nm. It is assumed that shell sliding does not occur between the nanotube core and outer housing. The deformation behavior for this assumption corresponds to the schematic illustration in inset of Figure 7a. Also, the NT Young's modulus is assumed to be 0.6 TPa. The actuation force was offset from NT midpoint to account for asymmetry in the device geometry caused by assembly inaccuracy. The behavior predicted by this model is summarized in Figure 7. It can be seen that the simulated deformation profile along the NT length is significantly different from the experimental profile in the region near the right anchor point. In addition, the pull-in voltage estimated by this approach is 6.6 V.

Next, we investigate the possibility of shell sliding at the anchor points as illustrated in the inset of Figure 8a. In this case, the finite-element model permits sliding along the axial direction while fully constraining transverse deflections at the anchor points. The rest of the model boundary conditions remain identical to those employed in the previous approach. The results from this approach are summarized in Figure 8. It can be seen that the deflection profile predicted by this model closely matches the experimental data. The pull-in voltage is estimated to be 5.8 V. In addition, the intershell sliding at anchor points is estimated to be 0.2 nm for the peak transverse deflection of 8.9 nm.

Table 1 summarizes the results from the two approaches, and shows that shell sliding is a more accurate approximation of the physical system when compared with experimental data. Two metrics are defined to assess the accuracy of these models. The first metric is the deviation in pull-in voltage ($D_{\text{pull-in}}$ (%)), which is defined as $D_{\text{pull-in}}$ (%) = $(V_{\text{model}} - V_{\text{exp}})/V_{\text{exp}} \times 100$, where V_{exp} represents the experimental pull-in voltage of 5.9 V, and V_{model} denotes the value predicted by simulations. The second metric is the deviation in the deformation profile (D_{def} (rms)), which is computed as the root-mean-square value of the difference between experimental data and modeling results.

From the summary in Table 1, the model with shell sliding at mechanical anchor points provides a better estimate of device performance. Of the two parameters that are used for comparing the simulation approaches, the deformation profile is more accurate. This is because the pull-in voltage estimated by the model is dependent on the value assumed for the Young's modulus. However, the nature of deformation exhibited by

TABLE 1. Comparison between Models

parameter	model without shell sliding	model with shell sliding
$D_{\text{pull-in}}$ (%)	11.9%	1.7%
D_{def} (rms)	0.55 nm	0.29 nm
elastostatic restoring force (nN)	325	185

the NT along its length is dependent solely on the boundary conditions and is independent of the Young's modulus value. This supports the argument that shell sliding does occur in this NT structure and the assumed average value of 0.6 TPa for the NT Young's modulus within our sample is accurate (since it provides a closer match to the experimental data for the model with shell sliding). This value of Young's modulus is also in agreement with measurements reported in previous efforts.[6,7,27,28] Thus, we have demonstrated the possibility of using NT shell engineering to tune not only its diameter but, also its mechanical clamping configuration at anchors resulting in low power device operation.

CONCLUSIONS

We have presented an overview of the electrostatic actuation and electromechanical switching behavior of 1-D nanoconstructs based on MWNTs. We have demonstrated three-state switching performance at low-power and identified the key failure modes of these devices. Comprehensive device models that take into account the nonlinearities induced by stress-stiffening of 1-D nanowires at large deformations have been developed. These models, which combine analytical techniques with finite-element methods, provide accurate estimates of device switching metrics such as switching voltage and pull-in gap. In addition to switching behavior, the simulations provide important new insights into the increased travel range that can be obtained when nanoscale elements are employed as strain absorbing elements in electrostatic actuators. This represents a significant performance improvement over the microscale counterparts used in conventional MEMS devices. Finally, we demonstrate the possibility of using NT shell engineering to tune the NT stiffness and nanomechanical clamping configuration in order to create low-power actuators/switches.

METHODS

Nanofabrication Procedure. The device fabrication process is as follows. First, the lower layer of four spatially separated metal electrodes (15 nm Cr/45 nm Au) is defined using E-beam lithography and metal lift-off. This is followed by dielectrophoretic assembly[19,30−32] of individual NTs onto the nanoelectrodes. We employ composite (AC+DC) fields to assemble individual NTs from a suspension in ethanol. In the next step, the nanotubes are imaged in an SEM and their position relative to the electrode midpoints (shifts caused by assembly inaccuracies) is measured. This is done to correctly locate the actuation electrodes on either side of the NT in the mask designs for the upper electrode. Next, the top metal contacts and actuation electrodes (15 nm Cr/75 nm Au) are defined using a second e-beam lithography step. The thickness of the metal layer defined in the second lithography step is designed to be higher than that defined within the first layer by 30 m. This is done to ensure that the actuation electrodes are higher than the suspended nanotubes, thereby eliminating the possibility of increased actuation gaps. Further information on the nanoassembly and hybrid nanofabrication procedure can be found in ref 19.

Device Characterization. The devices were characterized in vacuum within an on-wafer probe station from Desert Cryogenics. During measurements, the probe station was evacuated to 2 $\times$ 10^{-6} Torr using a combined Varian SD-40 prepump and Varian Turbo-V 70 turbo pump. Electrical connections to the device bonding pads were accomplished with 150 μm pitch GSG probes from Picoprobe. A precision semiconductor parameter analyzer (model 4156B) from Hewlett-Packard was used to generate electrical signals for actuation/switching and monitor device performance. MATLAB scripts embedded in a graphical interface were employed to control the parameter analyzer and acquire data.

Matlab Algorithm for Deformation Profile Extraction. The data was extracted by analyzing the images in Matlab with their Image Processing Toolbox. The images were initially processed using a 5 $\times$ 5 median filter to reduce noise, and then using the Canny edge detector.[39] The anchor points of the nanotube were subsequently selected by the user and a search line was created between these two points. At each pixel along this line, the perpendicular was searched for the maximum edge value in both directions. These two end points enabled the determination of the diameter and midpoint of the nanotube. After all end points were determined, the initial search line was refined based on the estimated midpoints. The final deflection and diameter profile information was determined from this estimated line and filtered with a one-dimensional median filter with a kernel length of 3.

Supporting Information Available: Further information is provided on the following aspects: (1) imaging artifacts associated with scanning electron microscopy of fabricated nanostructures, and (2) device failure modes. This material is available free of charge *via* the Internet at http://pubs.acs.org.

REFERENCES AND NOTES

1. Iijima, S. Helical Microtubules of Graphitic Carbon. *Nature* **1991**, *354*, 56–58.
2. Novoselov, K. S.; Geim, A. K.; Morozov, S. V.; Jiang, D.; Zhang, Y.; Dubonos, S. V.; Grigorieva, I. V.; Firsov, A. A. Electric Field Effect in Atomically Thin Carbon Films. *Science* **2004**, *306*, 666–669.
3. Juhasz, R.; Elfstrom, N.; Linnros, J. Controlled Fabrication of Silicon Nanowires by Electron Beam Lithography and Electrochemical Size Reduction. *Nano Lett.* **2005**, *5*, 275–280.
4. Xiang, B.; Wang, P. W.; Zhang, X. Z.; Dayeh, S. A.; Aplin, D. P. R.; Soci, C.; Yu, D. P.; Wang, D. L. Rational Synthesis of p-Type Zinc Oxide Nanowire Arrays Using Simple Chemical Vapor Deposition. *Nano Lett.* **2007**, *7*, 323–328.
5. Prinz, V. Y.; Seleznev, V. A.; Gutakovsky, A. K.; Chehovskiy, A. V.; Preobrazhenskii, V. V.; Putyato, M. A.; Gavrilova, T. A. Free-Standing and Overgrown InGaAs/GaAs Nanotubes, Nanohelices, and Their Arrays. *Phys. E* **2000**, *6*, 828–831.
6. Treacy, M. M. J.; Ebbesen, T. W.; Gibson, J. M. Exceptionally High Young's Modulus Observed for Individual Carbon Nanotubes. *Nature* **1996**, *381*, 678–680.
7. Poncharal, P.; Wang, Z. L.; Ugarte, D.; de Heer, W. A. Electrostatic Deflections and Electromechanical Resonances of Carbon Nanotubes. *Science* **1999**, *283*, 1513–1516.
8. Stampfer, C.; Helbling, T.; Obergfell, D.; Schoberle, B.; Tripp, M. K.; Jungen, A.; Roth, S.; Bright, V. M.; Hierold, C. Fabrication of Single-Walled Carbon Nanotube-Based Pressure Sensors. *Nano Lett.* **2006**, *6*, 233–237.
9. Jensen, K.; Kim, K.; Zettl, A. An Atomic-Resolution Nanomechanical Mass Sensor. *Nature Nanotechnol.* **2008**, *9*, 533–537.
10. Sazonova, V.; Yaish, Y.; Ustunel, H.; Roundy, D.; Arias, T. A.; McEuen, P. L. A Tunable Carbon Nanotube Electromechanical Oscillator. *Nature* **2004**, *431*, 284–287.

11. Jensen, K.; Weldon, J.; Garcia, H.; Zettl, A. Nanotube Radio. *Nano Lett.* **2007**, *7*, 3508–3511.
12. Fennimore, A. M.; Yuzvinsky, T. D.; Han, W. Q.; Fuhrer, M. S.; Cumings, J.; Zettl, A. Rotational Actuators Based on Carbon Nanotubes. *Nature* **2003**, *424*, 408–410.
13. Ke, C. H.; Espinosa, H. D. In Situ Electron Microscopy Electromechanical Characterization of a Bistable NEMS Device. *Small* **2006**, *2*, 1484–1489.
14. Lee, S. W.; Lee, D. S.; Morjan, R. E.; Jhang, S. H.; Sveningsson, M.; Nerushev, O. A.; Park, Y. W.; Campbell, E. E. B. A Three-Terminal Carbon Nanorelay. *Nano Lett.* **2004**, *4*, 2027–2030.
15. Jang, J. E.; Cha, S. N.; Choi, Y.; Amaratunga, G. A. J.; Kang, D. J.; Hasko, D. G.; Jung, J. E.; Kim, J. M. Nanoelectromechanical Switches with Vertically Aligned Carbon Nanotubes. *Appl. Phys. Lett.* **2005**, *87*, 163114.
16. Kaul, A. B.; Wong, E. W.; Epp, L.; Hunt, B. D. Electromechanical Carbon Nanotube Switches for High-Frequency Applications. *Nano Lett.* **2006**, *6*, 942–947.
17. Dujardin, E.; Derycke, V.; Goffman, M. F.; Lefevre, R.; Bourgoin, J. P. Self-Assembled Switches Based on Electroactuated Multiwalled Nanotubes. *Appl. Phys. Lett.* **2005**, *87*, 193107.
18. Kinaret, J. M.; Nord, T.; Viefers, S. A Carbon-Nanotube-Based Nanorelay. *Appl. Phys. Lett.* **2003**, *82*, 1287–1289.
19. Cha, S. N.; Jang, J. E.; Choi, Y.; Amaratunga, G. A. J.; Kang, D.-J.; Hasko, D. G.; Jung, J. E.; Kim, J. M. Fabrication of a Nanoelectromechanical Switch Using a Suspended Carbon Nanotube. *Appl. Phys. Lett.* **2005**, *86*, 083105.
20. Eriksson, A.; Lee, S.; Sourab, A. A.; Isacsson, A.; Kaunisto, R.; Kinaret, J. M.; Campbell, E. E. B. Direct Transmission Detection of Tunable Mechanical Resonance in an Individual Carbon Nanofiber Relay. *Nano Lett.* **2008**, *8*, 1224–1228.
21. Subramanian, A.; Dong, L. X.; Tharian, J.; Sennhauser, U.; Nelson, B. J. Batch Fabrication of Carbon Nanotube Bearings. *Nanotechnology* **2007**, *18*, 075703.
22. Collins, P. C.; Arnold, M. S.; Avouris, P. Engineering Carbon Nanotubes and Nanotube Circuits Using Electric Breakdown. *Science* **2001**, *292*, 706–709.
23. Huang, J. Y.; Chen, S.; Jo, S. H.; Wang, Z.; Han, D. X.; Chen, G.; Dresselhaus, M. S.; Ren, Z. F. Atomic-Scale Imaging of Wall-by-Wall Breakdown and Concurrent Transport Measurements in Multiwall Carbon Nanotubes. *Phys. Rev. Lett.* **2005**, *94*, 236802.
24. Subramanian, A.; Choi, T. Y.; Dong, L. X.; Tharian, J.; Sennhauser, U.; Poulikakos, D.; Nelson, B. J. Local Control of Electric Current Driven Shell Etching of Multiwalled Carbon Nanotubes. *Appl. Phys. A-Mater. Sci. Process.* **2007**, *89*, 133–139.
25. Jackson, J. D., *Classical Electrodynamics;* 3rd ed.; Wiley: New York, 1998.
26. Dequesnes, M.; Rotkin, S. V.; Aluru, N. R. Calculation of Pull-in Voltages for Carbon-Nanotube-Based Nanoelectromechanical Switches. *Nanotechnology* **2002**, *13*, 120–131.
27. Witkamp, B.; Poot, M.; van der Zant, H. S. J. Bending-Mode Vibration of a Suspended Nanotube Resonator. *Nano Lett.* **2006**, *6*, 2904–2908.
28. Huttel, A. K.; Poot, M.; Witkamp, B.; van der Zant, H. S. J. Nanoelectromechanics of Suspended Carbon Nanotubes. *New J. Phys.* **2008**, *10*, 095003.
29. Ke, C.; Espinosa, H. D.; Pugno, N. Numerical Analysis of Nanotube Based NEMS Devices—Part II: Role of Finite Kinematics, Stretching, and Charge Concentrations. *J. Appl. Mech.* **2005**, *72*, 726–731.
30. Dequesnes, M.; Tang, Z.; Aluru, N. R. Static and Dynamic Analysis of Carbon Nanotube-Based Switches. *J. Eng. Mater. Technol.* **2004**, *126*, 230–237.
31. Henrard, L.; Hernandez, E.; Bernier, P.; Rubio, A. Van der Waals Interaction in Nanotube Bundles: Consequences on Vibrational Modes. *Phys. Rev. B* **1999**, *60*, R8521–R8524.
32. Wong, L. H.; Zhao, Y.; Chen, G. H.; Chwang, A. T. Grooving the Carbon Nanotube Oscillators. *Appl. Phys. Lett.* **2006**, *88*, 183107.
33. Jones, J. E. L. Perturbation Problems in Quantum Mechanics. *Proc. R. Soc. A* **1930**, *129*, 598–615.
34. Guan, P.; McKenzie, D. R.; Pailthorpe, B. A. MD Simulations of Ag Film Growth Using the Lennard-Jones Potential. *J. Phys.: Condens. Matter* **1996**, *8*, 8753–8762.
35. Girifalco, L. A.; Hodak, M.; Lee, R. S. Carbon Nanotubes, Buckyballs, Ropes, and a Universal Graphitic Potential. *Phys. Rev. B* **2000**, *62*, 13104–13110.
36. Chung, J. Y.; Lee, K. H.; Lee, J. H.; Ruoff, R. S. Toward Large Scale Integration of Carbon Nanotubes. *Langmuir* **2004**, *20*, 3011–3017.
37. Liu, Y. L.; Chung, J. H.; Liu, W. K.; Ruoff, R. S. Dielectrophoretic Assembly of Nanowires. *J. Phys. Chem. B* **2006**, *110*, 14098–14106.
38. Krupke, R.; Hennrich, F.; Weber, H. B.; Kappes, M. M.; von Lohneysen, H. Simultaneous Deposition of Metallic Bundles of Single-Walled Carbon Nanotubes Using AC-Dielectrophoresis. *Nano Lett.* **2003**, *3*, 1019–1023.
39. Canny, J. A Computational Approach to Edge Detection. *IEEE Trans. Pattern Anal. Mach. Intell.* **1986**, *8*, 679–714.